Oxygen Formation During Stellar Helium Burning

Alexander Hewitt Young

Table of Contents

Acknowledgements

I would like to thank, first and foremost, my research advisor, Dr. Moshe Gai. This work would not have been possible without his continued support and guidance. I would like to thank him for getting me interested in experimental physics and the field of nuclear astrophysics. His dedication to his students is an inspiration and I have truly enjoyed working with him. I would also like to thank Dr. Henry Weller, Dr. Mohammed Ahmed, and Dr. Sean Stave at TUNL and Dr. Mark Spraker, Dr. Ralph France, and Dr. Richard Prior at North Georgia College and State University. Working with them at TUNL has shown me the sense of community among physicists and inspired me to pursue a Ph.D. in physics. Thank you to all the graduate students, post-docs, and professors at the University of Connecticut that have made completing this degree one of the best experiences of my life.

Abstract

An Optical Readout Time Projection Chamber (O-TPC) will be used in an experiment at the High Intensity γamma Source (HIγS) facility at Duke University for studying oxygen formation during stellar helium burning. The C/O ratio at the end of helium burning determines whether a Type II supernova yields a black hole (oxygen rich star) or a neutron star (carbon rich star). The C/O ratio is poorly known since the fusion of carbon plus helium is ill determined. We propose to resolve this problem with the use of the O-TPC that was constructed at the University of Connecticut (UConn).

The calibration of the O-TPC was carried out at the Laboratory for Nuclear Science (LNS) at Avery Point and subsequently the detector was transferred to the Triangle Universities Nuclear Laboratory (TUNL) at Duke in August 2007. A variety of pre-amplifiers and high voltage power supplies were used and under stable conditions an energy resolution as good as 2.6% was found in the charge signal. Charge and light gain curves were obtained using a ^{148}Gd source (3.1827 MeV α-particles) and a 7.5 cm diameter photo-multiplier tube (PMT) placed at approximately 85 cm. These determined the optimal conditions for operating the O-TPC. Under the optimized conditions a CCD camera was used to capture images of single and double tracks of alpha particles from a ^{148}Gd source. The 3.18 MeV alpha particles yielded tracks containing only 40-50 photo-electrons due to the small lens currently in use. The calibration results obtained at UConn were reproduced after the detector was installed at TUNL. The O-TPC is now in use for in beam experiments at the HIγS facility.

Ch. 1: Stellar Evolution

1.1 Energy Production

Stars are massive gaseous bodies that contain mostly hydrogen and helium and are powered by nuclear fusion in their cores. These gaseous bodies generate heat by gravitational contraction and the amount of heat gained is proportional to the amount of mass that is compressed in their cores. [Cla68, Rol68]

In Stellar Evolution we consider the Hertzsprung-Russell (H-R) diagram which depicts the star luminosity as a function of its temperature. These are determined using standard astronomical observables, such as magnitude (Fig. 1.1)[Shu82]. The path of evolution with regards to the H-R diagram depends on the mass of the star. Most stars fall along a band called the Main Sequence. Main Sequence stars undergo core hydrogen burning. When the hydrogen is exhausted the stars move along the subgiant and red giant branches of the H-R diagram and when the core becomes hot enough, helium burning starts. The helium burning stage takes the stars along the horizontal branch of the H-R diagram and their next stage of evolution depends on their mass. A low-mass star will eventually become a white dwarf, via the path shown in Fig. 1.2, while a high mass star ($M > 8\ M_\odot$) will undergo a core collapse Type II supernova explosion and become a neutron star or black hole. In this study we examine one of the important conditions, the carbon-oxygen ratio, that determines whether a Type II supernova will leave behind a black hole or a neutron star.
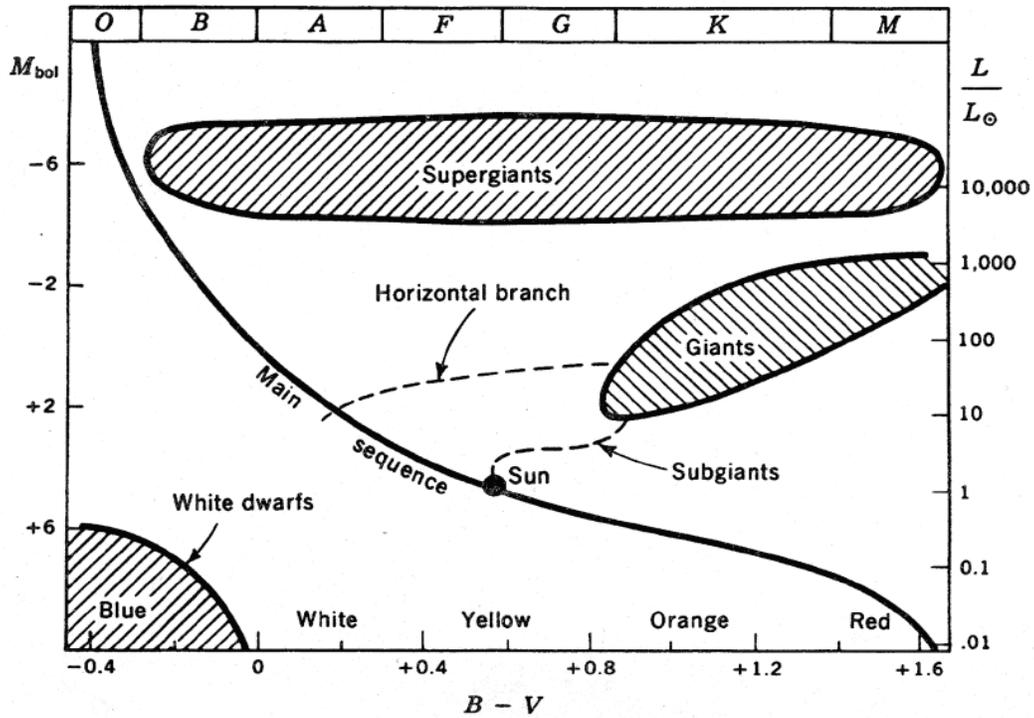
Fig 1.1: A Hertzsprung-Russel diagram depicting the main sequence, subgiant branch, and horizontal branch for the evolutionary path of the Sun.
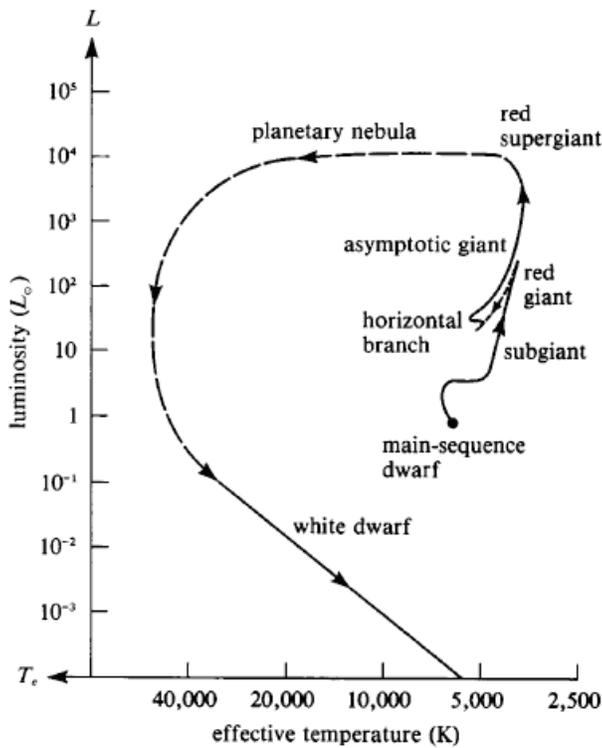
Fig. 1.2: An H-R diagram from [Sh82] depicting the evolution of a sun-like star of 1 $M_\odot$.

7

1.2 Nuclear Astrophysics

The nuclear reactions that are most important in stars involve collisions among ions with positive charges. The Coulomb force between the like charges causes a repulsion that can only be overcome if the colliding particles have sufficient energy. The high temperature of stellar cores can provide the particles with sufficient energy for nuclear fusion.

The Coulomb barrier, V_{CB}, is the energy that is required in classical physics to overcome the Coulomb repulsion and is given by the equation:

$$V_{CB} = \frac{Z_1 Z_2 e^2}{R} \approx \frac{Z_1 Z_2}{\sqrt[3]{A_1} + \sqrt[3]{A_2}} MeV \qquad (1)$$

where Z and A represent the atomic number and mass, respectively, of particles 1 and 2 and R is the classical distance between the particles.

Stars exhibit thermodynamic equilibrium and the velocities of stellar nuclei are given by the Maxwell-Boltzmann velocity distribution:

$$\phi(v) = 4\pi v^2 \left(\frac{m}{2\pi kT} \right)^{\frac{3}{2}} \exp\left(-\frac{mv^2}{2kT} \right) \qquad (2)$$

The Maxwell-Boltzmann distribution indicates that some of the nuclei will have much higher velocity than the average and can undergo nuclear reactions. Due to quantum tunneling, some nuclei can penetrate the coulomb barrier at energies less than indicated in (1).

The cross-section is the probability that a nuclear reaction will occur and is given by Bethe and Gamow parameterization [Cla68, Rol68] as:

$$\sigma(E) = \frac{S(E)}{E} \exp(-2\pi\eta) \qquad (3)$$

The Sommerfeld parameter (η) is given by $\eta = \frac{Z_1 Z_2 e^2}{\hbar v} = Z_1 Z_2 \frac{\alpha}{\beta}$, where $\acute{a} = \frac{e^2}{\hbar c}$, $\hat{a} = \frac{v}{c}$,

and S(E) represents the astrophysical cross section factor. The overlap of the Maxwell-Boltzmann distribution and the coulomb penetration term is referred to as the Gamow window and represents the most efficient energies for stellar burning. This is shown in Fig. 1.3 for the $^{12}C(p,\gamma)^{13}N$ reaction. Here we use standard nuclear reaction nomenclature indicating the target (^{12}C), the beam (p), the detected particle (γ), and the residual nucleus (^{13}N).
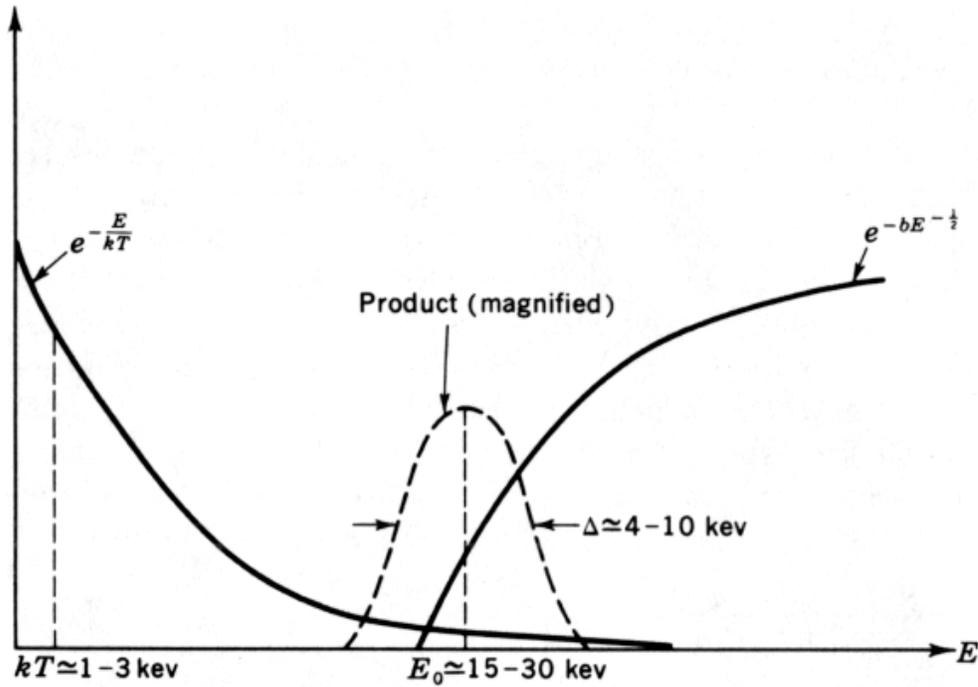
Fig. 1.3: The Gamow window for the $^{12}C(p,\gamma)^{13}N$ reaction.

Since the reaction cross sections at low energies are very small, significant extrapolation is needed from the results of high energy experiments. The S-factor, unlike the cross section, does not vary greatly with energy, which makes it ideal for

extrapolation. Thus, there is great interest in inspecting the S-factor, rather than the cross section, for a given nuclear reaction.

1.3 Burning stages

The major thermonuclear reactions in stars can be distinguished as a series of burning stages [Cla68, Rol68]. In all stars, there is an initial stage in which hydrogen (protons) fuse to form helium (α-particles). Once the hydrogen is exhausted, the core contracts due to self-gravitation. This causes an increase in temperature and density that allows the helium burning stage to begin.

Helium burning is the second stage of nuclear fusion and produces mainly ^{12}C and ^{16}O [Fow84]. Thermonuclear reactions that burn heavier and heavier elements require higher and higher temperatures and densities. Stars of less than 8 M$_\odot$ do not proceed with any burning stages beyond that of helium. They become carbon-oxygen white dwarfs and spend the rest of their lives radiating the pressure energy of electron degeneracy.

The more massive stars experience further core contraction which allows carbon burning, in which a neon and oxygen core is formed. This pattern of core contraction and burning continues until eventually silicon burning creates an iron core, which cannot undergo nuclear fusion. The iron cannot fuse to form heavier elements, so it begins to aggregate until it reaches the Chandrasekhar limit of 1.4 M$_\odot$ [Cha84]. When the star reaches this mass limit, the pressure outwards can no longer overcome the gravitational force inwards and it undergoes a core collapse Type II supernova explosion.

It is important to note that after the core exhausts hydrogen the layers of the star outside the core reach temperatures that allow further hydrogen burning to occur. These

reactions form a shell surrounding the new core, which undergoes the next stage of nuclear fusion. These shell-ignition stages occur after each core-ignition stage. An illustration of a progenitor star of 25 $M_\odot$ is given in Fig. 1.4.
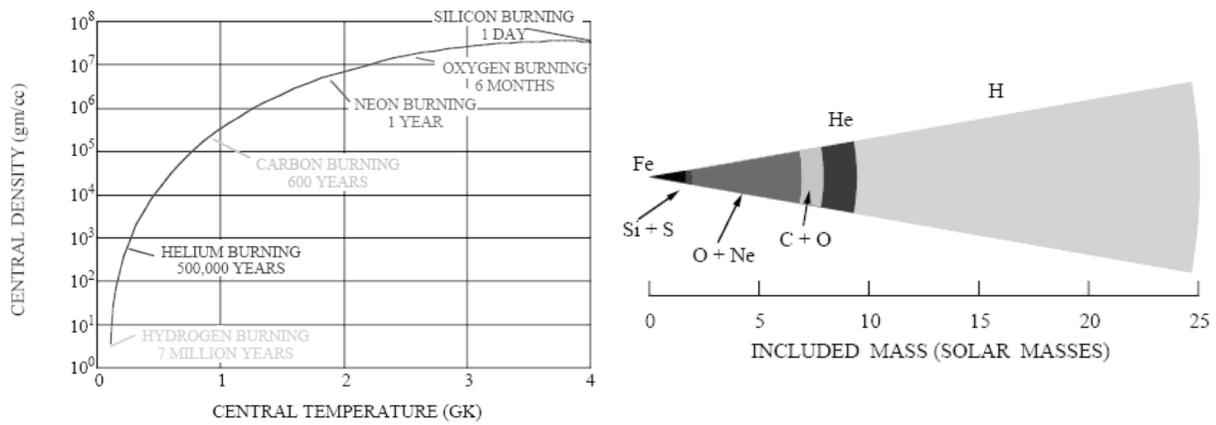
Fig. 1.4: The various burning stages of a progenitor star of 25 $M_\odot$ [Be85]. The lower figure is a corrected version of the one made by Bethe and Brown, who incorrectly labeled the x-axis by a factor of 10 [Gai99].

1.3.1 Hydrogen Burning

During hydrogen burning, a chain of reactions occurs that converts H nuclei into ^{4}He. The chain of reactions that occurs depends strongly on the mass of the star. The low mass stars with core temperatures below 17 MK, such as the sun, undergo the p-p chain while more massive stars undergo the C-N-O cycle (Fig. 1.5) [Bet68]. These reactions continue until all of the hydrogen in the core has been converted to helium.

The helium core, which is denser than its hydrogen counterpart, converts gravitational energy to thermal energy as it contracts. This leads to an increase in temperature to 200 MK where helium burning begins.

	P-P chains	C-N-O cycle
PPI	$^{1}_{}H + {}^{1}H \rightarrow {}^{2}D + e^{+} + {}^{0}_{0}í_{e}$ $^{2}D + {}^{1}H \rightarrow {}^{3}He + {}^{0}_{0}ã$ $^{3}He + {}^{3}He \rightarrow {}^{4}He + 2\,{}^{1}H$	$^{12}_{6}C + {}^{1}_{1}H \rightarrow {}^{13}_{7}N + {}^{0}_{0}ã$ $^{13}_{7}N \rightarrow {}^{13}_{6}C + {}^{0}_{1}e + {}^{0}_{0}í$
PPII	$^{3}He + {}^{4}He \rightarrow {}^{7}Be + {}^{0}_{0}\gamma$ $^{7}Be + e^{-} \rightarrow {}^{7}Li + {}^{0}_{0}\nu_{e}$ $^{7}Li + {}^{1}H \rightarrow 2\,{}^{4}He$	$^{13}_{6}C + {}^{1}_{1}H \rightarrow {}^{14}_{7}N + {}^{0}_{0}ã$ $^{14}_{7}N + {}^{1}_{1}H \rightarrow {}^{15}_{8}O + {}^{0}_{0}ã$
PPIII	$^{7}Be + {}^{1}H \rightarrow {}^{8}B + {}^{0}_{0}\gamma$ $^{8}B \rightarrow {}^{8}Be + e^{+} + \nu_{e}$ $^{8}Be \rightarrow 2\,{}^{4}He$	$^{15}_{8}O \rightarrow {}^{15}_{7}N + {}^{0}_{1}e + {}^{0}_{0}í$ $^{15}_{7}N + {}^{1}_{1}H \rightarrow {}^{12}_{6}C + {}^{4}_{2}He$
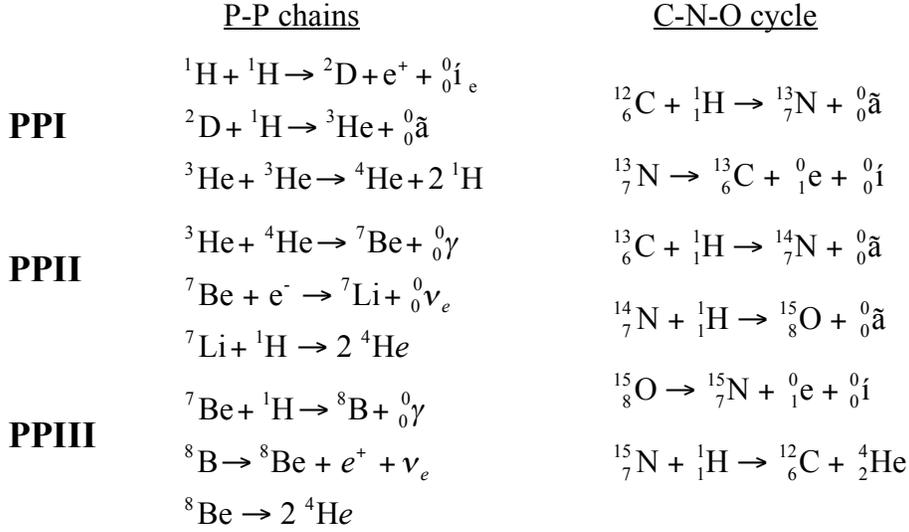
Fig 1.5: Three stages of the P-P chain and the C-N-O cycle. In both reactions ^{4}He is formed from H.

1.3.2 Helium Burning

During helium burning, the two primary reactions that occur are the triple alpha process that creates carbon and, subsequently, the $^{12}C\,(\alpha, \gamma)\,^{16}O$ reaction that creates oxygen [Fow84] [Wea93]:

$$\text{Triple-}\alpha\text{ Process} \left\{ \begin{array}{l} ^{4}_{2}He + {}^{4}_{2}He \rightarrow {}^{8}_{4}Be + {}^{0}_{0}ã \\[2mm] ^{8}_{4}Be + {}^{4}_{2}He \rightarrow {}^{12}_{6}C + {}^{0}_{0}ã \end{array} \right.$$

$$^{4}_{2}He + {}^{12}_{6}C \rightarrow {}^{16}_{8}O + {}^{0}_{0}ã \tag{7}$$
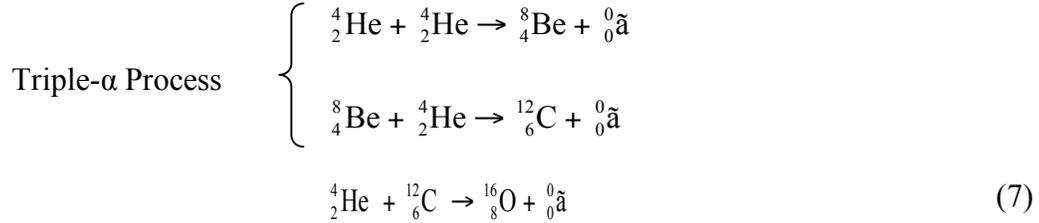
According to (1) the coulomb barrier for the $^{12}C\,(\alpha, \gamma)\,^{16}O$ reaction is approximately 3 MeV which is far greater than the average kinetic energy of particles in the star, which is approximately 25 keV. Quantum tunneling and Maxwell-Boltzmann distribution allow the reaction to take place. The most efficient energy for this reaction, the Gamow window, is approximately 300 keV.

The helium burning stage is vital in determining the result of the Type II supernova explosion. Specifically, the ratio of carbon to oxygen produced during helium burning determines whether or not the star collapses to a black hole. If very little carbon is produced the star skips the carbon and neon burning stage, shown in Fig. 1.4, and proceeds directly to oxygen burning [Wea93]. This results in a larger, hotter iron core that will collapse to a black hole. Thus, the understanding of stellar evolution hinges on an accurate understanding of the carbon to oxygen ratio during helium burning.

1.4 Death of a star

Early in the 20th century, Edwin Hubble discovered that the universe was expanding. He was able to calculate distances to nearby galaxies using Cepheid variable stars and Vesto Slipher made measurements of the redshifts of these galaxies [Sli13]. Hubble compared the redshift and distance measurements to obtain a plot of velocity vs. distance for these galaxies, shown in Fig. 1.6. This comparison allowed Hubble to conclude that the universe was expanding and determined the expansion constant, known as the Hubble constant, to be 500 km/s/Mpc [Hub36]. Due to errors in his distance calibration, this value is approximately seven times larger than the accepted value today, but the importance of his discovery is that the universe is expanding.

Type Ia (SNeIa) is a supernova that results when a carbon-oxygen white dwarf accretes mass from a red giant. The white dwarf gains enough mass to reach the Chandrasekhar limit of 1.4 $M_\odot$ which results a SNeIa explosion. SNeIa is of great importance in cosmology because a star which explodes in this fashion releases a known amount of light [Phi93] which is equal to that of an entire galaxy. Thus, when we observe a galaxy approximately doubling its luminosity over a few weeks period it is
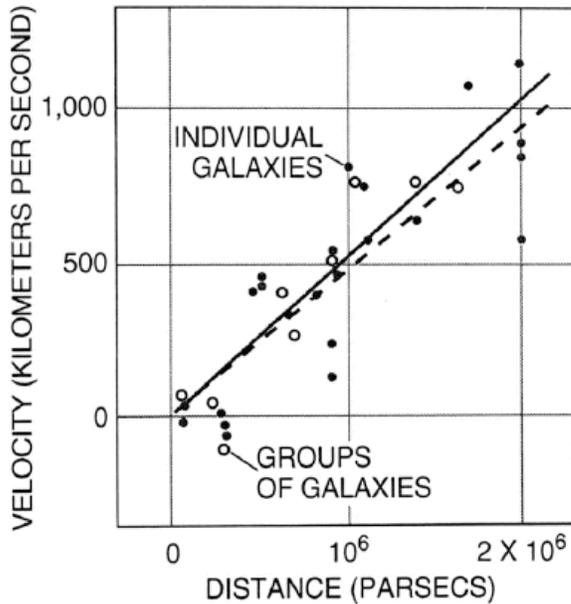
Fig 1.6: Hubble's comparison of velocity and distance for the 46 nearest galaxies.

likely that a SNeIa has occurred there. The distance to the galaxy can be determined [Phi93] based on the observed luminosity of this explosion and an empirical determination of the absolute luminosity from its light curve.

The understanding of the luminosity of a Type Ia supernova explosion depends on the initial carbon-oxygen mixture of the white dwarf. Currently, the luminosity of a SNeIa is formed by the empirical Phillips relationship [Phi93] and in order to place it on firm theoretical foundation we need to formulate a complete theory of stellar evolution including the carbon-oxygen ratio of the initial white dwarf.

At the end of the 20th century, observations made by the Hubble Space Telescope of SNeIa [Per99, Rei98] indicated that very distant galaxies were less luminous than was predicted by the Hubble expansion from near galaxies. Thus, these galaxies are further away than we expect, and the expansion of the universe must be accelerating due to a phenomena that has been dubbed dark energy. This is one of the most exciting

14

discoveries in physics in the last century and has given rise to theories concerning dark energy and dark matter.

Ch. 2: Previous Experiments

2.1 Previous Experiments

Extensive work has been done in an attempt to accurately determine the S-factor and rate of the ^{12}C (α, γ) ^{16}O reaction in stellar helium burning [Gai99]. Laboratory experiments in this endeavor tend to agree for large energies, but are unable to make accurate measurements below energies of approximately 1.5 MeV. Since the most efficient energy for the ^{12}C (α, γ) ^{16}O reaction in stars is approximately 300 keV, previous experiments require significant extrapolation.

The extrapolation in this case is troublesome. There are two states with spin parity of 1$^-$ in ^{16}O that can be reached via the collision of ^{12}C and an alpha-particle. One state is the quasi-bound 1$^-$ state (at 9.63 MeV) and the other is the bound 1$^-$ state (at 7.12 MeV). The quantum mechanical tail of the bound state extends to positive energies. Thus, there is an interference between the quasi-bound and bound 1$^-$ states, which leads to two possible values for the cross section at 300 keV. If the states exhibit constructive interference there will be a larger cross section while destructive interference results in a smaller cross section.

2.2 Beta-delayed alpha particle emission

One of the methods that attempted to indirectly measure the S-factor of the ^{12}C (α, γ) ^{16}O reaction is to measure the beta-delayed alpha particle emission of ^{16}N. This is the process by which ^{16}N beta decays to ^{16}O followed by alpha-particle decay. Experiments in beta-delayed alpha particle emission of ^{16}N were conducted by Yale-

UConn [Zha93, Fra96, Fra97], TRIUMF [Buc93], and Argonne National Lab [Tan07]. The results disagree with regards to both data and theory.

The TRIUMF group suggests that the S-factor is 79 keV-b and the Argonne group suggests a value of 74 keV-b. Hale's [Hal97] analysis of the available data result a value closer to 10 keV-b (Fig. 2.1). Clearly, the extrapolation from β-delayed α-particle emission cannot adequately determine the cross section at low energies. We propose to perform a direct measurement of the cross section at low energies.
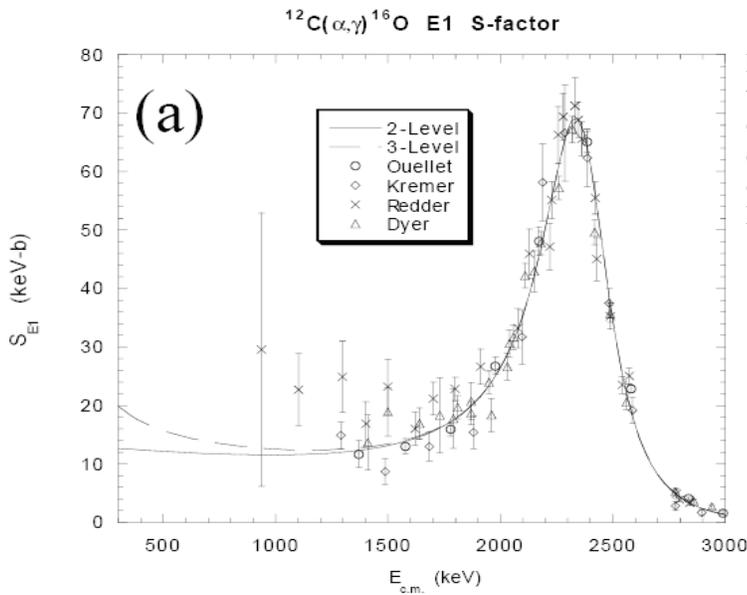
Fig. 2.1: Calculated S-factor for two-level and three-level fits compared with measurements by β-delayed α-particle emission. Values of approximately 10 keV-b and 20 keV-b are predicted. [Ha97].

2.3 Direct gamma-ray measurements

Direct measurements of the $^{12}C(\alpha,\gamma)^{16}O$ reaction at low energies are not experimentally viable due to the high background. The most recent attempt to measure the direct reaction at low energies was made by J. W. Hammer *et al.* [Ham06]. Representative spectra measured at 1.850 MeV are shown as published in Fig. 2.2 where the peaks are indiscernible due to the large background.

16
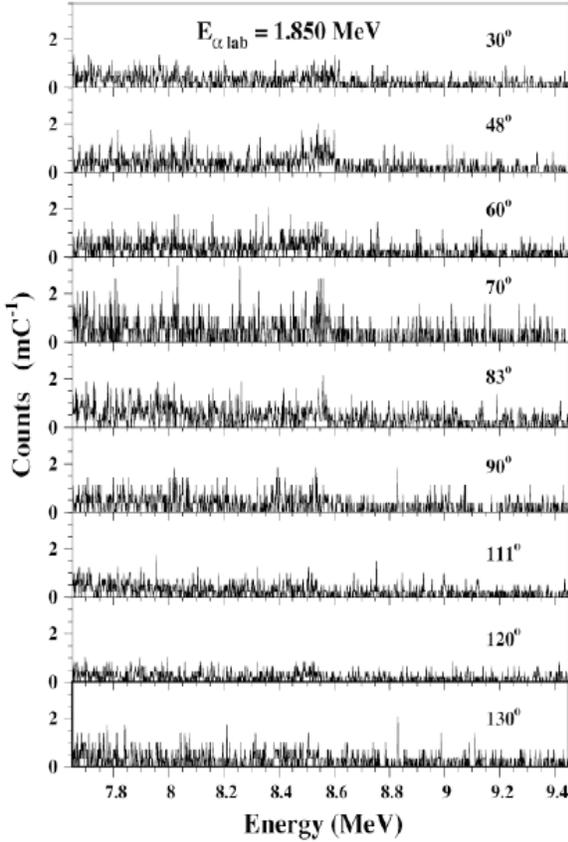
Fig. 2.2. γ spectra of the $^{12}C(\alpha,\gamma)^{16}O$ reaction for $E_{CM} = 1.305$ MeV for the angular range $30°$-$130°$ from [Ham06].

2.4 $^{16}O(\gamma,\alpha)^{12}C$

In order to determine the astrophysical S-factor for the $^{12}C(\alpha,\gamma)^{16}O$ reaction, it is useful to study the time reverse reaction, $^{16}O(\gamma,\alpha)^{12}C$. This reaction has a larger cross-section (Fig. 2.3), and for a similar luminosity it will yield a larger number of events.

$$\acute{o}(\tilde{a},\acute{a}) = \frac{(2S_1 +1)(2S_2 +1)}{2(2S_4 +1)} x\sigma(\alpha,\gamma)$$

$$\acute{o}(\tilde{a},a) = \frac{(2S_1 +1)(2S_2 +1)}{1(2S_4 +1)} \ x \ \frac{k_{\acute{a}}^2}{k_{\tilde{a}}^2} \ x \ \acute{o}(\acute{a},\tilde{a}_i)$$

$$but : \sigma(\alpha,\bar{\gamma}_i) = \frac{1}{2}\sigma(\alpha,\gamma)$$

$$= \frac{(2S_1 +1)(2S_2 +1)}{2(2S_4 +1)} \ x \ \frac{k_\alpha^2}{k_\gamma^2} \ x \ \sigma(\alpha,\gamma)$$

$$= \frac{1}{2} \ x \ (80-160) \ x \ \sigma(\alpha,\gamma)$$

$$\boxed{= (40-80) \ x \ \sigma(\alpha,\gamma)}$$

Fig. 2.3: Calculation of the cross-section of $^{16}O(\gamma,\alpha)^{12}C$ compared to the cross-section of $^{12}C(\alpha,\gamma)^{16}O$. The cross-section of the reaction we propose to examine is 40-80 times larger than the inverse reaction studied in previous experiments.

17

Ch. 3: The Detector

3.1 Overview of the apparatus
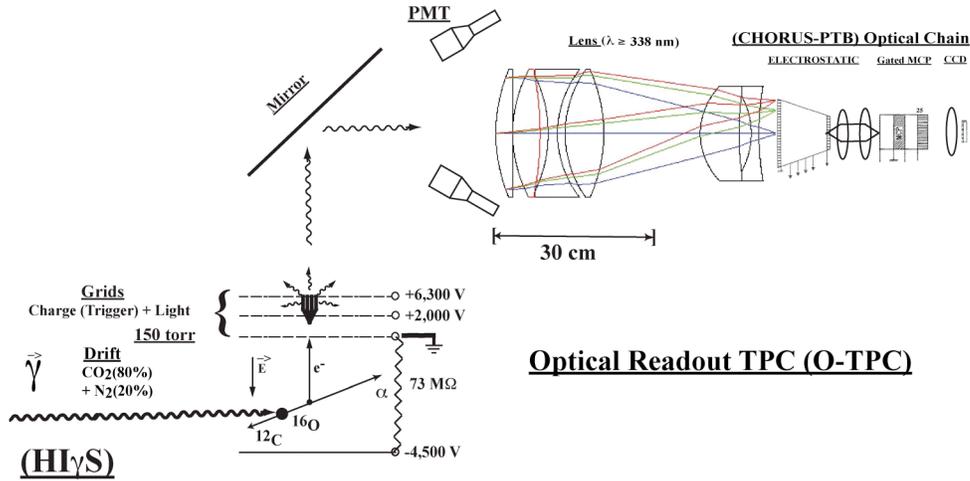
Fig. 3.1: A schematic diagram of the O-TPC.

The O-TPC consists of a time projection chamber (TPC) with an optical readout system (Fig. 3.1). Gamma rays are sent into a chamber filled with a gas mixture of 80% CO_2 and 20% N_2. The gammas cause photodissociation of ^{16}O and produce ^{12}C and α particles. As the ^{12}C and α particles travel through the chamber they release delta electrons that generate secondary ionization electrons. The potential difference between the cathode at the base of the TPC and the first grid (at ground potential) creates an electric field pointing downward that causes the ionization electrons to drift upwards. After passing through the first grid, the electrons undergo an avalanche process and are multiplied by approximately 10^4, where they can be detected as a charge signal. The avalanche electrons then pass the second grid and react with the nitrogen gas to produce light, which is sent through the optical system.

The optical system consists of a mirror followed by a UV lens, electrostatic demagnifier, multi-channel plate (MCP), and cooled CCD Camera, as well as two PMTs.

The light that enters the optical system travels first through the UV lens where it is focused onto the photocathode of the Hamamatsu V4440U electrostatic demagnifier. The demagnifier, with a diameter of 100 mm, focuses the light onto a screen in the back with a 25 mm diameter, as shown in Fig. 3.1, so it can enter the MCP. The MCP is triggered to only register events of interest and it amplifies the light signal into an image that can be recorded by the CCD camera. Some of the light from the TPC is also picked up by the PMTs to yield the time projection signals (Fig. 3.2) that allow for a measurement of the azimuthal angle of the tracks.
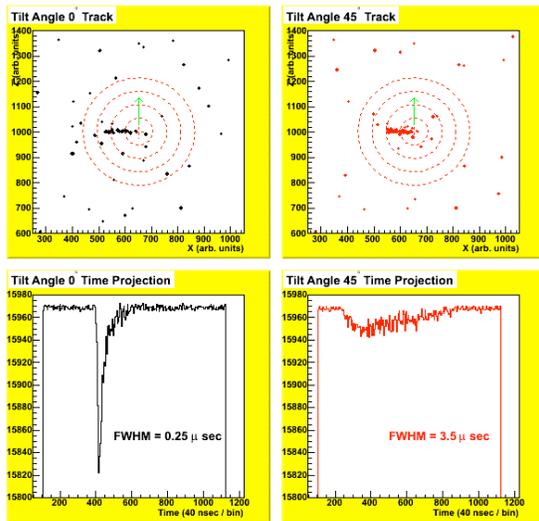
Fig. 3.2: PMT time projection signals for a 0° track (left) and a 45° track (right).

Ch. 4: Experimental Procedure

4.1 Calibration of Drift Field

The voltage of the cathode determines the potential difference, and thus the strength of the electric field, in the chamber. This drift field determines the number of electrons that drift through the upper grids to be multiplied and converted to light. We are interested in losing as few electrons in the drift volume as possible so a calibration of the drift field was necessary.

4.2 Gain of Light and Charge

The electron multiplication and light production is heavily influenced by the electric field in the regions between grids. After the electrons drift through the first grid, they gain energy from the electric field between the first and second grids. These higher energy electrons cause an avalanche, and more electrons are produced. As the electric field increases the number of these interactions increases and a larger avalanche is achieved.

In this calibration, the first grid was kept at ground while the second and third grid voltages, V_2 and V_3 respectively, were adjusted. In each test, V_2 was held fixed while V_3 was varied. The calibration was performed for V_2=0.5-3.0kV and V_3=4.5-7.0kV.

4.3 Tracks Recorded at Avery Point

The photo-electrons produced from the tracks of α-particles from ^{148}Gd traveled through the optical chain and were recorded by the CCD camera. The total number of photo-electrons can be estimated by simple examination of the images.

The trigger is created from a valid grid (charge) signal with energy above 1.0 MeV. This trigger opens the MCP gate and projects an image on the back screen of the MCP. This image is recorded by the CCD camera. The number of photo-electrons recorded heavily depends on the gate width of the MCP. Therefore, a calibration of the gate is necessary to determine the optimal settings for the experiment. An examination of track images was performed for gate widths of 50μs, 100μs, 500μs, and 2000μs.

4.4 Charge Resolution

In order to achieve results of high accuracy it is important to have the best possible resolution of charge signals. The design-goal for charge resolution was 3%. In

order to achieve this resolution the components of the O-TPC such as cables, pre-amplifiers, and power supplies had to be tested and replaced as necessary.

Ch. 5: Results

5.1 Optimal Drift Field

Fig. 5.1 shows the calibration curve obtained from the study of the drift field. The cathode voltage, V_0, was varied from 1.01kV to approximately 5.60kV with the first grid at ground. The output of the charge signal increased from 63.4 channels to its saturated value of approximately 168 channels above 4.8kV.
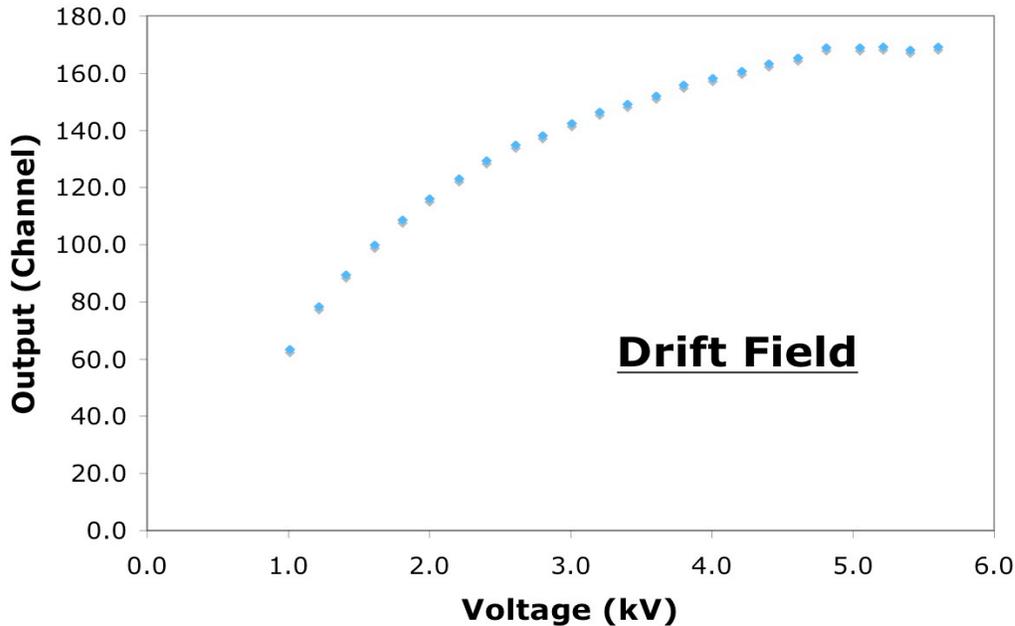
Fig. 5.1: The charge output as the drift field was varied.

The results of the drift field calibration indicate that the maximum charge output occurs at $V_0 \approx 4.8$kV. At $V_0 > 4.8$kV the output does not increase dramatically, which indicates complete charge collection. The optimal condition for the cathode is the lowest voltage with the highest output. Therefore, the calibration indicates that the optimal cathode voltage is approximately 4.8kV.

5.2 Gain of light and charge

The calibration curves of charge gain and light production, Fig. 5.2, show very similar results for each value of V_2 that was tested. The highest gain in charge and number of photo-electrons produced occurred at $V_2 = 2.0$ kV and $V_3 \approx 6.4$ kV. Sparks occurred when V_2 was much lower than V_3 because the electric field became too strong. In order to avoid sparking, V_3 is set to a voltage slightly less than the maximum in the calibration curves. This ensures that high charge gain and photo-electron output is achieved with stable operation.
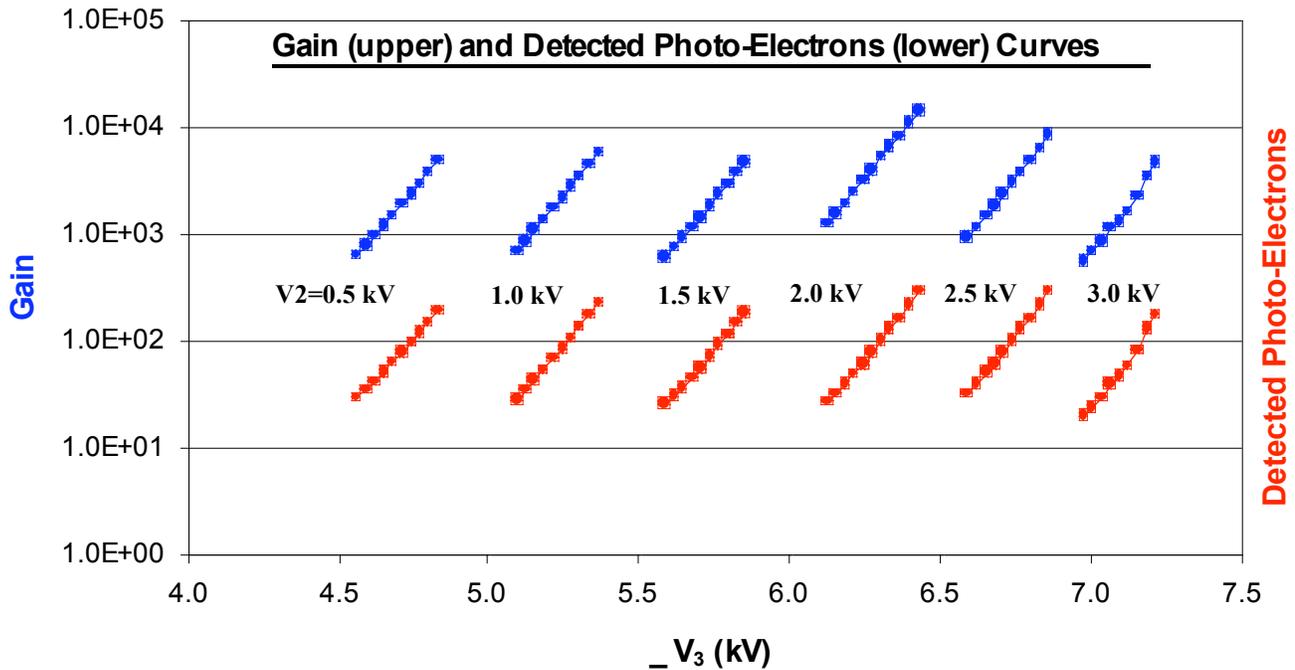
Fig. 5.2: An examination of the electron multiplication and light production as the voltages of grid 2 and grid 3 were varied. The upper curves represent the charge gain while the lower curves represent the number of photo-electrons detected.

5.3 Picture of Tracks

The tracks recorded at Avery Point contain, on average, 40-50 photo-electrons. Fig. 5.3 shows a one-track and two-track event with the Bragg maxima represented by the dense regions of photo-electrons at the end of the tracks.
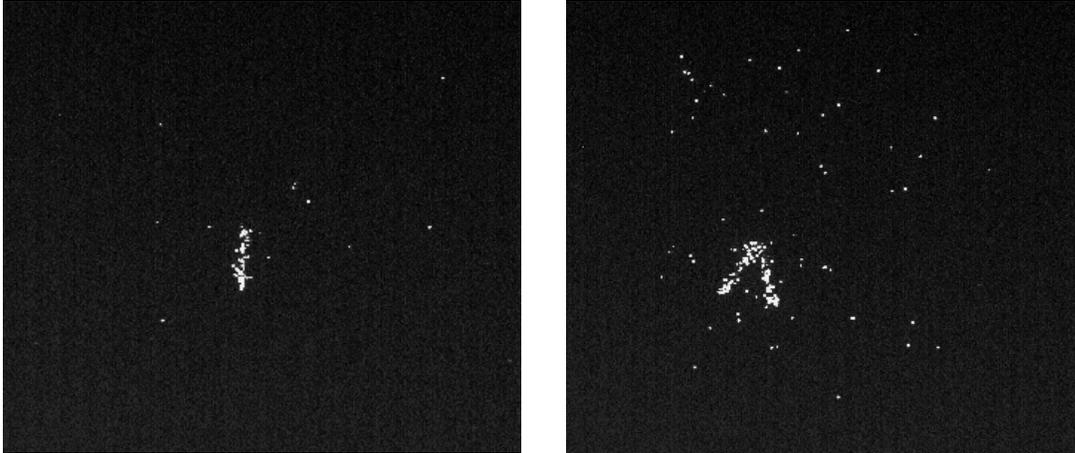
Fig. 5.3: Images taken by CCD camera of one track (left) and two tracks (right). Each track contains approximately 40-50 photo-electrons.

The number of photo-electrons recorded as a function of gate width is shown in Fig. 5.4. Tracks of approximately 25 photo-electrons were recorded with a 50µs gate width while tracks of 45 photo-electrons were recorded with the 2000µs gate width. A longer gate width, however, causes more background light to be collected as well (Fig. 5.5).
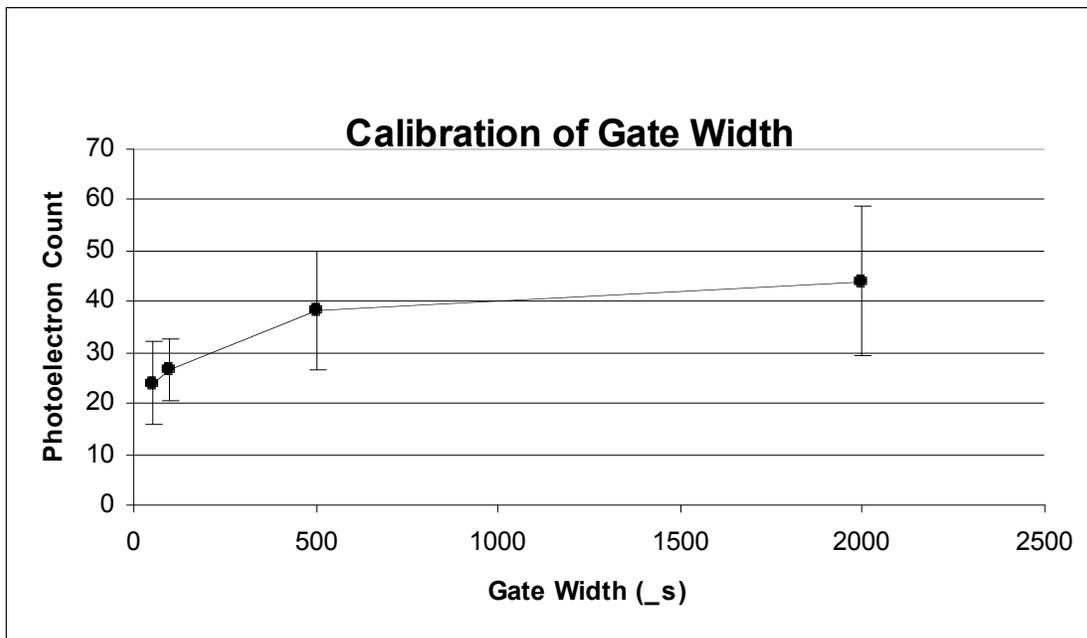
Fig. 5.4: The average number of photo-electrons produced as the gate width of the CCD camera was varied.
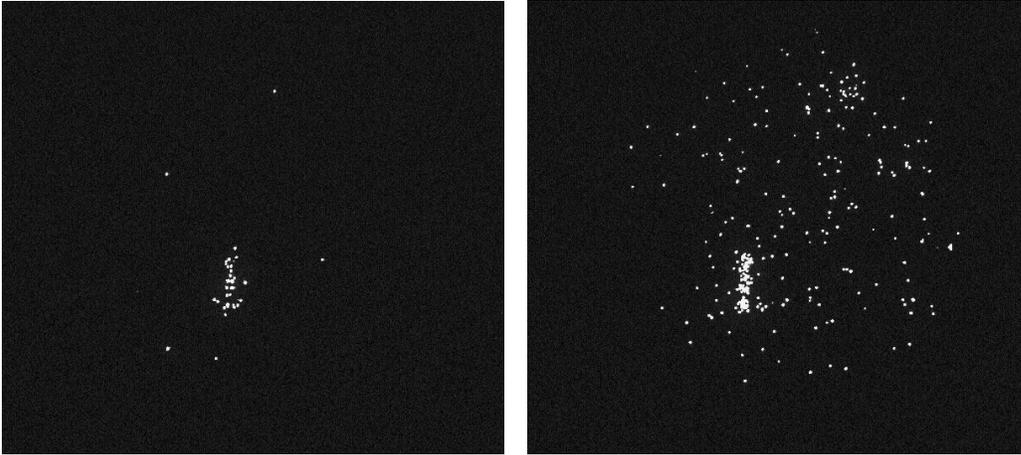
Fig. 5.5: Comparison of tracks recorded with gate width 50μs (left) and 2000 μs (right). The image on the right has a brighter track, but contains more background light.

5.4 Charge Resolution

The charge resolution of the O-TPC prior to calibration and fine-tuning was approximately 12%. After replacing pre-amplifiers, power supplies, and high voltage cables, a 2.6% resolution was obtained. As the PMT voltages were adjusted, the resolution of the light signals were improved as well. A typical set of histograms for the charge and light signals after fine-tuning is shown in Fig. 5.6.
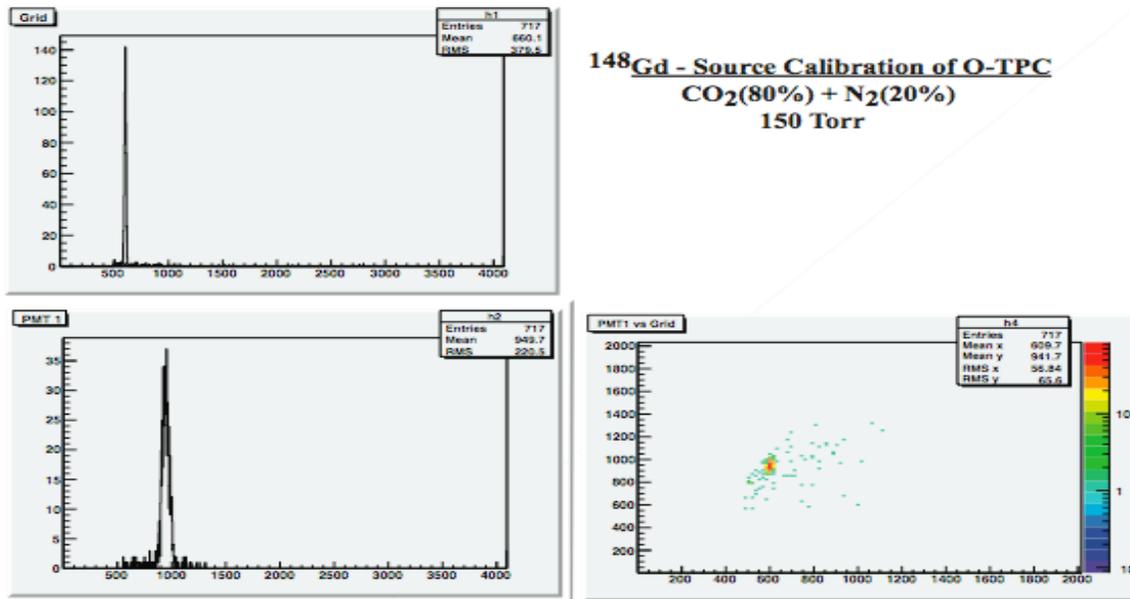
Fig. 5.6: Charge and light spectra of α-particles from a [148]Gd source.

24

Ch. 6: Transfer to TUNL

Following the calibration and performance testing discussed in this study, the O-TPC was transferred to TUNL at Duke University. The chamber and optical system were transported separately along with the large frame that had been constructed for the apparatus. The frame was built by the University of Connecticut Technical Services Center and allows the apparatus to be positioned at a height consistent with that of the HIγS beam. A special clean room and temporary lab was constructed at TUNL and the O-TPC was reassembled there. The reconstructed apparatus mounted on the frame is shown in Fig. 6.1.
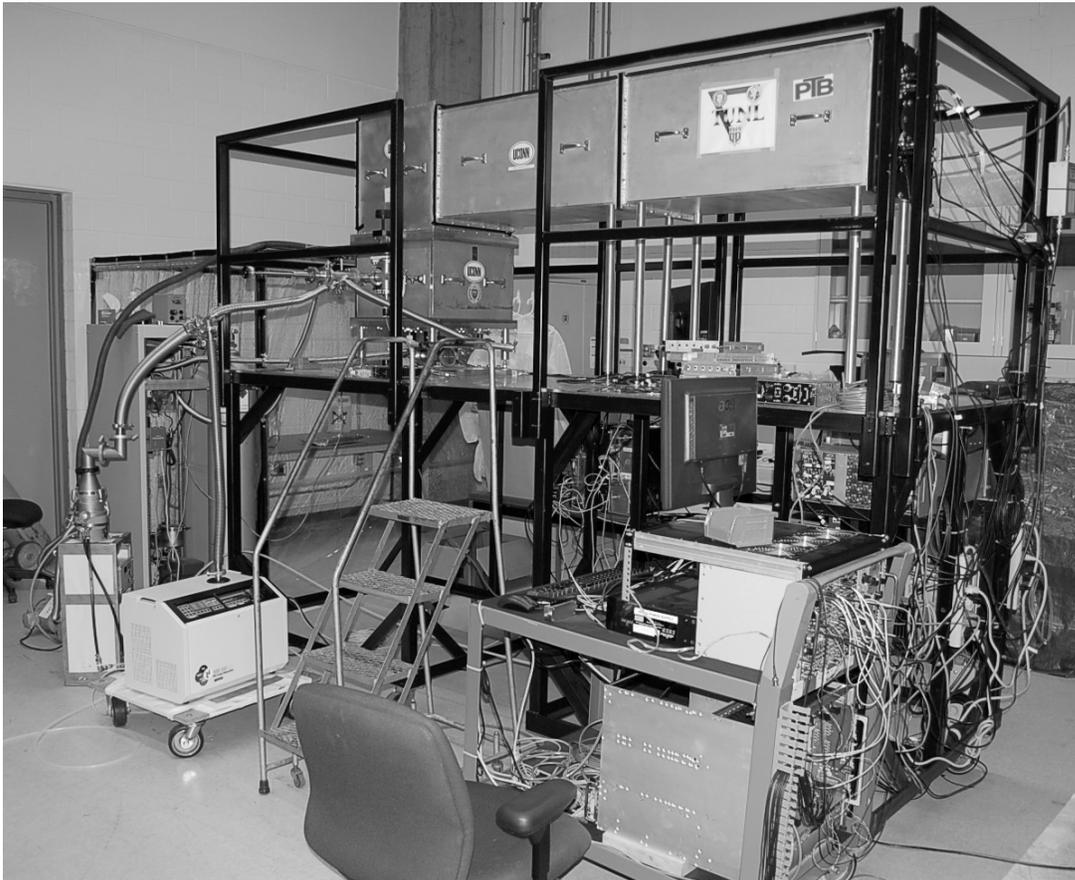
Fig. 6.1: The O-TPC mounted to the frame built at UConn with the data acquisition system (lower right) and gas handling system with leak detector (left).

Ch. 7: Conclusion

7.1 Summary of Results

The calibration and performance testing of the O-TPC indicated that the apparatus was ready to receive beam from HIγS. The optimal drift field was determined to be V_0=-4.8kV. The highest gain in charge and light occurred with V_2=2.0kV and V_3=6.4kV. With these settings the charge gain was approximately 10^4 and over 100 photo-electrons were detected in the PMTs. The CCD camera was found to record tracks of approximately 40-50 photo-electrons with good resolution so the optical chain was functioning well. The power supplies, pre-amplifiers, and cables were replaced as necessary and this improved the charge signal resolution from approximately 12% to approximately 2.6%, which exceeded the experimental goals. The calibration and fine-tuning of the O-TPC was successful and determined that it was ready for the experiment at HIγS.

7.2 *Current work*

In March 2008, the O-TPC was transported from the temporary lab at TUNL to the beam line at HIγS. The apparatus was tested for gas leaks and o-rings were replaced as necessary. The data acquisition system was configured for remote use from the HIγS control room. A test of the background noise in the room was carried out while another experiment was running on the beam line. The background was acceptable and the threshold was set to eliminate most of the noise. In the first week of April 2008, the O-TPC had its first engineering run and over 500 events were recorded. The data is currently being analyzed and some of the preliminary results are shown in Fig. 7.1. The

O-TPC awaits funding for further upgrades, such as a larger lens, and is being prepared

for future runs at HIγS.
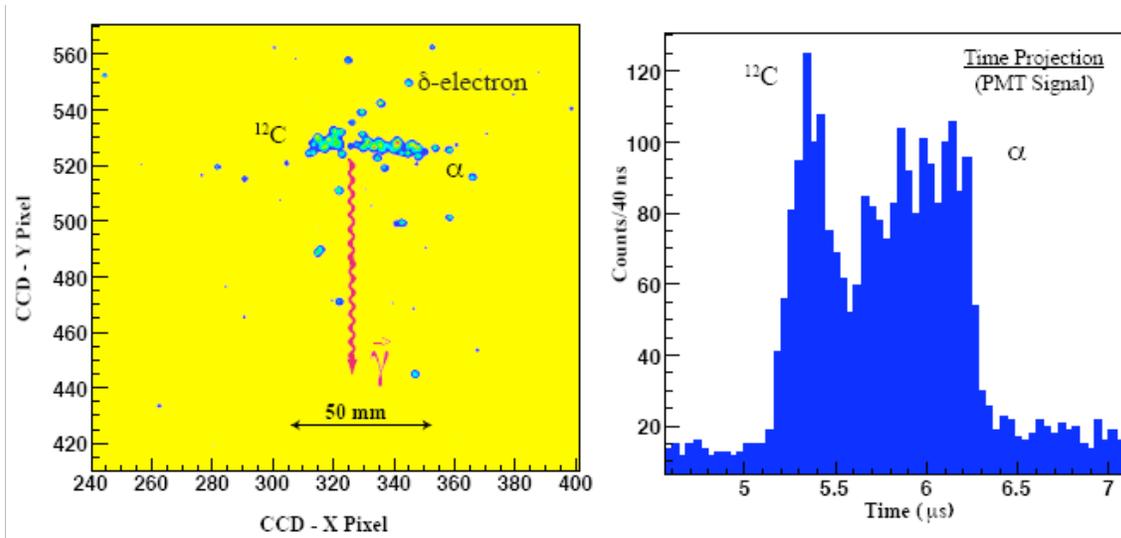
Fig. 7.1: First ^{12}C$(\alpha,\gamma)^{16}$O track recorded by the O-TPC at HIγS, March 31, 2008.

References

[Bet68] Hans A. Bethe, Physics Today, 21:9(1968)36.

[Buc93] L. Buchmann, R.E Azuma, C.A. Barnes, J.M. D'Auria, M. Dombsky, U. Giesen, K.P. Jackson, J.D. King, R.G. Korteling, J. Powell, G. Roy, J. Vincent, T.R. Wang, S.S.M. Wong, and P.R. Wrean; Phys. Rev. Lett. 70(1993)726.

[Cha84] S. Chandrasekhar, Rev. Mod. Phys. 56(1984)137.

[Cla68] Donald D. Clayton, Principles of Stellar Evolution and Nucleosynthesis, University of Chicago Press, 1968.

[Dye74] P. Dyer, Nuclear Physics A233(1974)495-520.

[Fow84] W.A. Fowler, Rev. Mod. Phys. 56(1984)149.

[Fra96] R.H. France III; Ph.D. thesis, Yale University, 1996.

[Fra97] R.H. France III, E.L. Wilds, N.B. Jevtic, J.E. McDonald, and M. Gai; Nucl. Phys. A621(1997)165c.

[Gai99] Moshe Gai, Summer School Lecture, 1999.

[Hal97] G.M. Hale; Nucl. Phys. bf A621(1997)177c.

[Ham06] J. W. Hammer, Phys. Rev C73 (2006).

[Hub36] E.P. Hubble, Silliman Lectures, Yale University, 1936.

[Per99] S. Perlmutter, G. Aldering, G. Goldhaber, R. A. Knop, P. Nugent, P. G. Castro, S. Deusta, S. Fabbro, A. Goobar, D. E. Groom, I. M. Hook, A. G. Kim, M. Y. Kim, J. C. Lee, N. J. Nunes, R. Pain, C. R. Pennypacker, and R. Quimby; Astrophys. Journal 517(1999)565-586.

[Phi93] M. Phillips, Astrophys. J. Lett. 413(1993)105.

[Reiss] Adam G. Riess, Alexei V. Filippenko, Peter Challis, Alejandro Clocchiatti, Alan Diercks, Peter M. Garnavich, Ron L. Gilliland, Craig J. Hogan, Saurabh Jha, Robert P. Kirshner, B. Leibundgut, M. M. Phillips, David Reiss, Brian P. Schmidt, Robert A. Schommer, R. Chris Smith, J. Spyromilio, Christopher Stubbs, Nicholas B. Suntzeff, and John Tonry; Astrophys. Journal 116(1998)1009-1038.

[Rol88] C.E. Rolfs, and W.S. Rodney; Cauldrons in the Cosmos, University of Chicago Press, 1988.

[Shu82] Frank H. Shu, The Physical Universe, University Science Books, 1982.

[Sli13] V. M. Slipher, The radial velocity of the Andromeda Nebula, Lowell Observatory Bulletin, 1(1913)56-57.

[Tan07] X. D. Tang, K. E. Rehm, I. Ahmad, C. R. Brune, A. Champagne, J. P. Greene, A. A. Hecht, D. Henderson, R. V. F. Janssens, C. L. Jiang, L. Jisonna, D. Kahl, E. F. Moore, M. Notani, R. C. Pardo, N. Patel, M. Paul, G. Savard, J. P. Schiffer, R. E. Segel, S. Sinha, B. Shumard, and A. H. Wuosmaa; Phys. Rev. Lett. 99, 052502 (2007).

[Wea93] T.A. Weaver, and S.E. Woosley; Phys. Rep. 227(1993)65.

[Zha93] Z. Zhao, R.H. France III, K.S. Lai, S.L. Rugari, M. Gai, and E.L. Wilds, Phys. Rev. Lett. 70(1993)2066, ER 70(1993)3524.

[Zha93] Z. Zhao, Ph.D. thesis, Yale University, 1993.